

Endothelin-3 and T-type Ca^{2+} channels drive enteric neural crest cell calcium activity, contractility and migration

Received: 3 July 2025

Accepted: 16 December 2025

Published online: 20 January 2026

 Check for updatesNicolas R. Chevalier¹✉, Fanny Gayda², Nadège Bondurand², Ze Chi Chan¹, Thierry Savy¹, Monique Frain¹, Amira El Merhie¹, Lenuta Canta³, Monica Dicu³, Isabelle Le Parco⁴ & Léna Zig¹

Enteric neural crest cells (ENCCs) colonize the gut during embryogenesis and migration defects give rise to Hirschsprung disease (HD). Mutations in GDNF/RET and EDN3/EDNRB are known to be causal in HD. Here, we show that migrating ENCCs in mice exhibit endogenous EDN3/EDNRB-gated calcium activity, mediated by chloride channels, T-type Ca^{2+} channels and inositol trisphosphate-sensitive intracellular-store release. We find that inhibiting Ca^{2+} activity results in ENCC migration defects, while exciting it promotes migration by increasing ENCC contractility and traction force to the extracellular matrix. Our study demonstrates that embryonic endothelin-mediated neural crest migration and adult endothelin-mediated vasoconstriction is one and the same phenomenon, taking place in different cell types. Our results suggest a functional link between rare mutations of *CACNA1H* (the gene encoding $\text{Ca}_v3.2$) and HD, and pave the way for understanding neurocristopathies in terms of neural crest cell bioelectric activity deficits.

Neural crest cells (NCC) are a population of multipotent, highly migratory cells common to all vertebrates. They colonize developing organs during embryonic development to give rise to a variety of structures including cranio-facial bone, chromaffin cells of the adrenal medulla, Schwann cells of the peripheral nervous system and the neurons and glia of the enteric nervous system (ENS). NCCs have attracted much scientific attention because of their paramount contributions to vertebrate physiological and pathological^{2,3} development, to domestication-induced phenotypes^{4,5} and because aberrantly expressed NCC developmental programs can lead to cancer tumor invasiveness^{6,7}. Vagal-derived⁸ enteric neural crest cells (ENCCs) invade the gut rostro-caudally between 9.5 and 13.5 days of development in mice to form the ENS. ENCC migration defects result in colonic aganglionosis at birth, a syndrome known as Hirschsprung disease (HD). HD is one of the most frequent neurocristopathies, affecting ~1:5000 births⁹. The mutations hitherto identified, mostly in the GDNF/RET^{10–12} and EDN3/EDNRB^{13,14} signaling cascades, are of

incomplete penetrance and account for only 50 % of the familial and 15–20 % of the sporadic cases¹⁵; the cause of most HD cases is today not understood. Bioelectric activity^{16–18}, as measured by Ca^{2+} imaging or membrane potential changes, is increasingly recognized as a key player of stem cell^{16–18} and NCC^{19–22} behavior. Spontaneous propagating Ca^{2+} waves in ENCCs²³ were found to depend on purinergic signaling, but their implication for migration and HD remained uncertain. Here, we show that most of the Ca^{2+} activity in ENCCs occurs as unsynchronized single-cell events and not as waves, that ENCC Ca^{2+} activity is driven by EDN3/EDNRB, via the opening of Cl⁻ and T-type Ca^{2+} channels, and that Ca^{2+} activity is intimately correlated with ENCC migration potential through a simple mechanism: elevated intracellular Ca^{2+} leads to increased ENCC contractility and traction force to the extracellular matrix that allows them to migrate down the gut. This mechanism renews our understanding of how EDN3/EDNRB affects ENCC migration. Disruption of any components of this mechanism can result in a NCC migration defect,

¹Laboratoire Matière et Systèmes Complexes, Université Paris Cité, CNRS UMR 7057, 10 rue Alice Domon et Léonie Duquet, Paris, France. ²Laboratory of Genetics of Developmental Disorders, Imagine Institute, INSERM UMR 1163, Université Paris Cité, 24 Boulevard du Montparnasse, Paris, France. ³UNIVO, 1 cour du Havre, Paris, France. ⁴Institut Jacques Monod, Université Paris Cité, CNRS, Paris, France. ✉e-mail: nicolas.chevalier@u-paris.fr

opening-up new perspectives for neurocristopathy and collective cell migration research.

Results

Enteric neural crest cells display spontaneous Ca^{2+} activity during gut invasion

We monitored Ca^{2+} activity (CA) on ex-vivo mouse embryonic guts expressing the intracellular Ca^{2+} reporter GCaMP6f specifically in NCCs (Fig. 1a, Supplementary Movie 1), and measured its spatial distribution and characteristics with an automated analysis pipeline (Fig. S1). CA in migrating ENCCs was spontaneous and occurred mostly as asynchronous, non-propagating, single-cell events. Ca^{2+} transients could sometimes propagate radially to neighboring cells, but such wave-like events²³ occurred, at E11.5, at an activity of $\text{CA}_{\text{wave}} = 7.5 \times 10^{-4} \pm 2 \times 10^{-4}$ events/min/100 μm^2 (\pm SEM, $n=15$), i.e. ~ 100 - 1000 times less frequently than single-cell events (Fig. 1b). Endogenous CA at the ENCC migration front decreased from E10.5 to E12.5 (Fig. 1b, Fig. S2, Supplementary Movie 1). At E11.5, it was significantly higher at the ENCC wavefront located at the ileo-cecal junction (ilcc) than in trailing ENCCs (Fig. 1c), concentrating at the cecum and antimesenteric ileum border (Figs. 1a and S3). CA was also present in transmesenteric ENCCs (Fig. S3). CA was insensitive to tetrodotoxin (Figs. 1d and S4), and therefore did not stem from neural activity; the latter could however be elicited by veratridine in proximal gut segments (Figs. 1e and S4). Endogenous CA co-localized with the ENCC-specific marker Sox10, but only very partially with the neuronal marker Tuj1 (Supplementary Movie 2). These results indicate that spontaneous CA originated in ENCCs and was most intense during early gut colonization stages, decreasing as ENCCs gradually differentiated to neurons and glia.

Endogenous Ca^{2+} activity is induced by EDN3/EDNRB

We next investigated whether the ligand/receptor pair EDN3/EDNRB involved in ENCC development was related to ENCC electric activity. Application of 1 nM EDN3 at E11.5 led to a threefold CA increase (Supplementary Movie 3, Figs. 2a and S5), while further addition of EDN3 had more variable effects, presumably caused by the exhaustion of Ca^{2+} reservoirs upon repeated stimulation with EDN3. In stage E12.5

ileum, CA also increased threefold at 1 nM EDN3 (Fig. S5), and the application of 10 nM EDN3 induced an immediate increase of intracellular Ca^{2+} across all ENCCs (Fig. 2b, Supplementary Movie 3, Fig. S5). Unlike EDN3, GDNF, the other major ligand involved in ENCC development, did not modify CA at the 10 ng/mL concentration known to drive ENCC chemotaxis²⁴ (Figs. 2c and S6). EDN3 is endogenously expressed by the gut mesenchyme, concentrating at the cecum and at the anti-mesenteric ileal border^{25,26}. This pattern mirrored the CA heatmaps we recorded (Figs. 1a and S3). We therefore blocked endogenous EDN3/EDNRB signaling with the EDNRB antagonist BQ788: it almost extinguished CA ($-77 \pm 14\%$, $n=14$) (Figs. 2d and S5, Supplementary Movie 4) for at least 24 h (Fig. 2e), while the drug vehicle, DMSO, did not affect CA (Fig. S7). In addition, BQ788 systematically led to a rounding of ENCCs and a retraction of their cell processes (Fig. 2f, Supplementary Movie 4). We finally tested whether CA differed in an EDN3 missense mutation model that develops Hirschsprung disease, the *Is/Is* mouse. Because this mouse didn't express GCaMP, we resorted to 1 day on-substrate-culture of intestinal explants in medium with GDNF and loaded the preparation with Fluo4-AM. The average frequency of ENCC Ca^{2+} transients was lower by $\sim 25\%$ in the *Is/Is* homozygote than in controls (Fig. 2g-i).

T-type Ca^{2+} channels and Cl^- channels mediate Ca^{2+} oscillations

We next investigated the ionic transport mechanisms leading to Ca^{2+} oscillations downstream of EDNRB. Removing extracellular Ca^{2+} with EDTA led to a complete cessation of CA (Fig. 3a, Supplementary Movie 5). Consistent with the requirement for extracellular Ca^{2+} , GdCl_3 , a cation channel blocker, significantly reduced CA (Figs. 3a and S8). Interestingly, transients could still be elicited by acute administration of EDN3 10 nM in the presence of EDTA (Figs. 3e and S9, Supplementary Movie 5), indicating a contribution of intracellular Ca^{2+} stores. 2-APB halted activity (Figs. 3a and S8) while ryanodine did not affect CA (Figs. 3a and S8). These findings show that both extracellular Ca^{2+} and intracellular IP₃, but not ryanodine-sensitive Ca^{2+} stores contribute to CA.

We further questioned the entry pathway of extracellular Ca^{2+} , first considering voltage-gated Ca^{2+} channels (VGCCs). The L-type Ca^{2+}

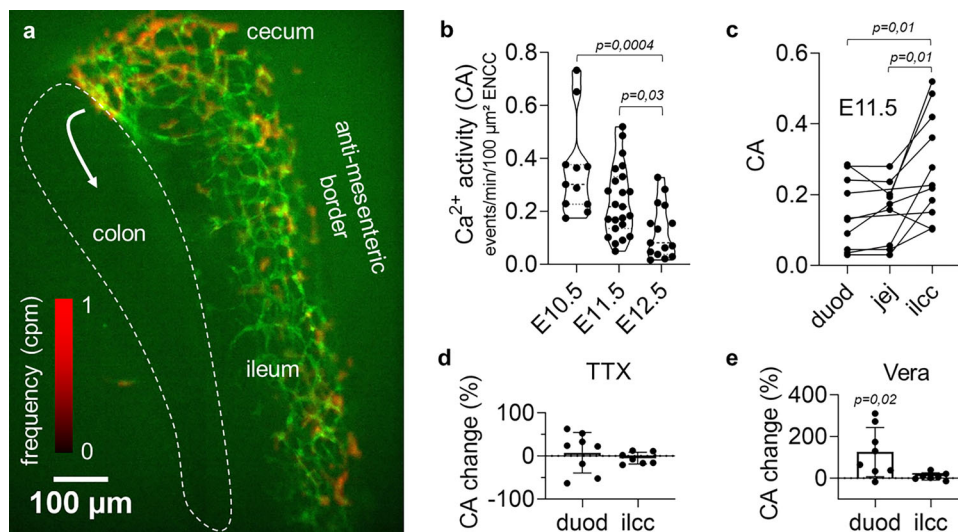


Fig. 1 | Endogenous Ca^{2+} activity in enteric neural crest cells during gut colonization. **a** Green: average time-projection of GCaMP6f time-lapse at the E11.5 ileo-cecal junction (Supplementary Movie 1); ENCCs have reached the cecum and are about to enter the colon (white arrow). Red: CA frequency heatmap shows concentration of activity at the cecum and the ileum anti-mesenteric border (see also Fig. S3). **b** CA at the ENCC migration front at stages E10.5 (jejunum, $n=11$), E11.5 (ileo-cecal junction, $n=23$), E12.5 (colon, $n=15$), Kruskal Wallis test. **c** CA in the

duodenum (duod), jejunum (jej) and ileo-cecal junction (ilcc) at E11.5. Lines link points measured from the same sample ($n=11$), two-tailed Wilcoxon matched pairs signed rank (WMP) test. **d** Tetrodotoxin (TTX, 1 μM) did not modify CA in the duodenum ($n=8$) or ilcc ($n=7$) at E11.5. **e** Veratridine (Vera, 10 μM) induced CA in the duodenum ($n=8$), but not in the ilcc ($n=7$) at E11.5, WMP test. All error bars are \pm SD.

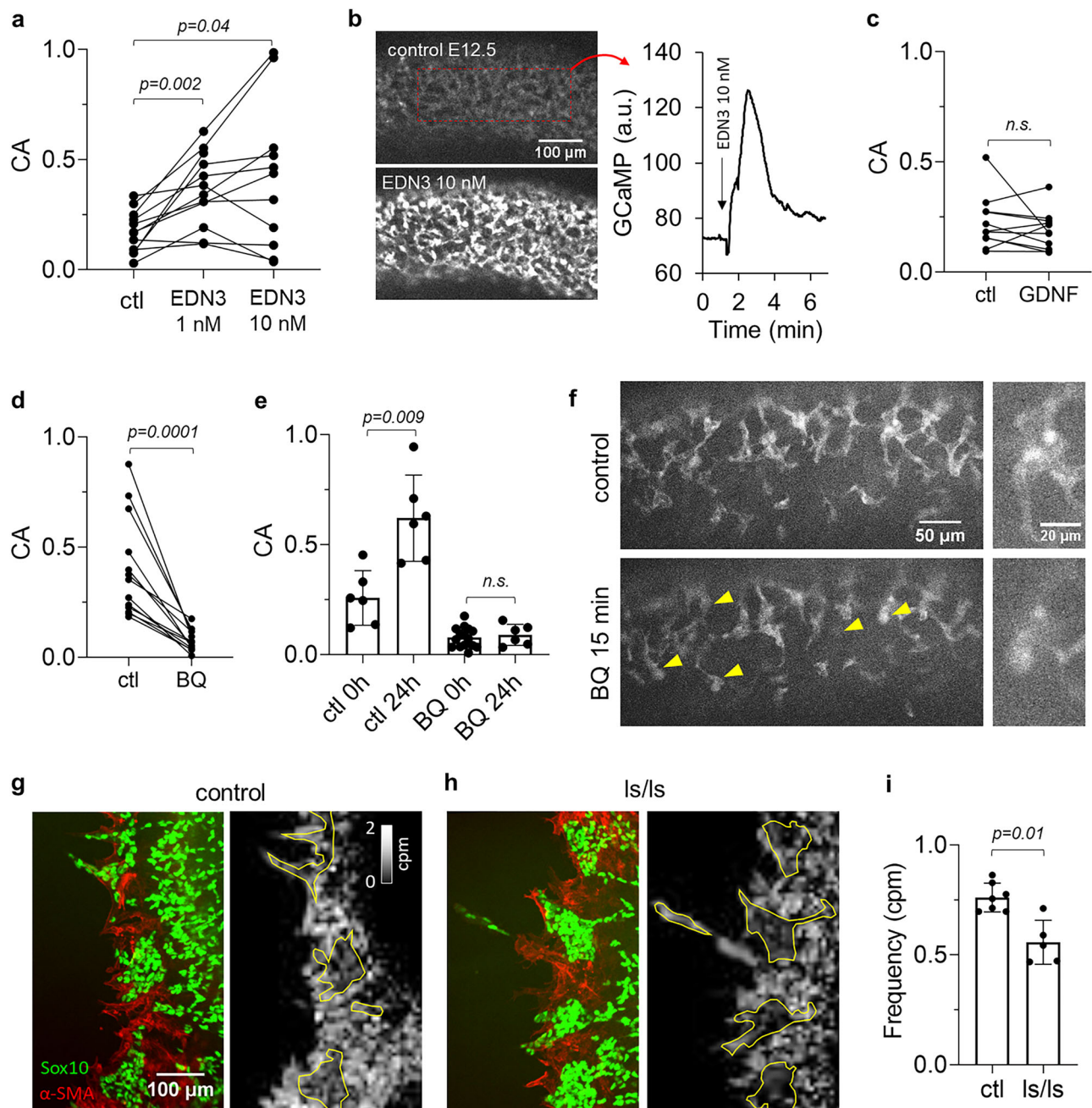


Fig. 2 | EDN3/EDNRB drives Ca^{2+} activity in ENCCs. **a** Effect of EDN3 1 and 10 nM on Ca^{2+} activity (CA) in E11.5 ilcc, $n = 12$, WMP test. **b** Sharp Ca^{2+} rise spanning all GCaMP positive cells after 10 nM EDN3 administration detected in 11/13 samples in E12.5 ileum (Supplementary Movie 3). Right panel: GCaMP signal intensity in the dashed red rectangle upon EDN3 introduction. The intracellular Ca^{2+} rise could not be stimulated again upon renewed application of 10 nM EDN3 ($n = 6/6$). **c** Effect of GDNF 10 ng/mL in E11.5 ilcc, $n = 11$, WMP test. **d** Effect of the EDNRB blocker BQ788 10 μM , E11.5 ilcc, $n = 14$, WMP test. **e** Evolution of CA in control ($n = 6$) and BQ 788 ($n = 6$) treated samples after 24 h in culture, two-tailed Mann Whitney test. Error bars are $\pm\text{SD}$. CA increase of control samples after 24 h culture does not reflect the physiological, stage-by-stage decrease of CA (Fig. 1b): this discrepancy could arise

from components of the medium, possibly serum. **f** Left: ENCC process retraction and cell rounding (yellow arrowheads) observed after 15 min incubation in BQ 788 (Supplementary Movie 4). Right: magnified appearance of a cell group before/after BQ 788 application. **g, h** Left panels: Sox10 and $\alpha\text{-SMA}$ immunohistochemistry of ENCCs and mesenchymal cells in control (heterozygote) and Is/Is sample. Right panels: registered heatmap of Ca^{2+} transient frequency, ENCC aggregate borders are shown in yellow as drawn from the IHC images. ENCCs display lower frequency than the mesenchyme. **i** Frequency of transients for $n = 7$ controls and $n = 5$ Is/Is, two-tailed Mann Whitney test. Each dot is a different sample/embryo and a line connects the same sample before and after drug application in all figures of this report. Error bars are $\pm\text{SD}$.

channel (CaV1.2) blocker nifedipine inhibits activity in fetal and adult ENS neurons²⁷ but did not significantly alter CA in E11.5 guts (Figs. 3b and S10). Ruthenium red, a non-selective blocker of P/Q-type (CaV2.1) and N-type (CaV2.2) channels as well as of cationic TRPV channels, did not affect CA either (Figs. 3b and S10). Blockade of all 3 T-type Ca^{2+} channels (CaV3.1,2,3) with Z944 induced a dose- and time-

dependent decrease of CA (Figs. 3b, S10, and S12, and Supplementary Movie 6). CaV3.2 (encoded by *Cacna1h*) is strongly expressed in E11.5 ENCCs²⁸; we found that specific blockade of CaV3.2 with ascorbic acid (AA) 1 mM²⁹ also induced a dose- and time-dependent decrease of CA (Figs. 3b, S10, and S12, and Supplementary Movie 6). The only commercially available T-type Ca^{2+} channel agonist, SAK3, is specific for

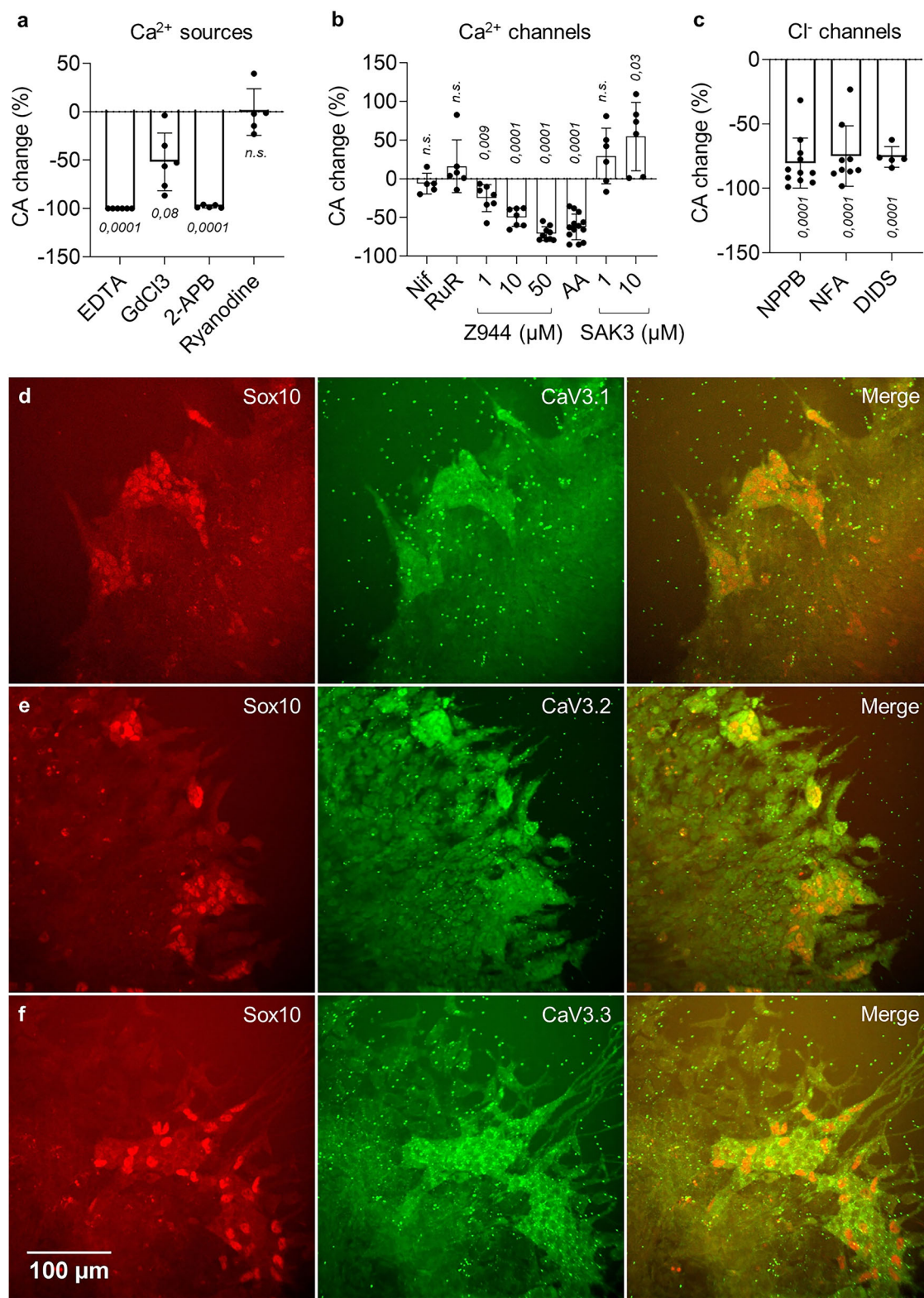


Fig. 3 | T-type Ca^{2+} channels and Cl^{-} channels are critical for Ca^{2+} oscillations. All experiments in (a–c) are performed at E11.5 at the ileo-cecal junction. Error bars are \pm SD. **a** CA change relative to control before drug application for EDTA (2 mM, $n = 6$), GdCl3 (100 μM , $n = 6$), 2-APB (100 μM , $n = 5$), ryanodine (10 μM , $n = 5$). **b** CA change for nifedipine (Nif, 10 μM , $n = 5$), ruthenium red (RuR, 100 μM , $n = 6$), Z944 at 1 μM ($n = 7$), 10 μM ($n = 7$), 50 μM ($n = 9$), ascorbic acid (AA, 1 mM, $n = 13$) and SAK3 at 1 μM ($n = 6$), 10 μM ($n = 6$). **c** CA change for NPPB (100 μM , $n = 11$), NFA (50 μM ,

$n = 9$) and DIDS (500 μM , $n = 5$). Two-tailed p -values for (a–c) are calculated from the Student t -test. Sox10 and CaV3.1 (d), CaV3.2 (e) and CaV3.3 (f) IHCs of ENCCs migrating from an intestinal explant on a substrate. All three T-type Ca^{2+} channels are expressed by ENCCs, but not by the surrounding mesenchymal cells. The small bright green dots are AF647 μ -beads fluorescing in the same range as the T-type Ca^{2+} channel secondary antibody. They were added in the overlying collagen gel for another experiment (see Fig. 6).

CaV3.1 and CaV3.3³⁰. This molecule induced a significant CA increase at 10 μM (Figs. 3b and S10, and Supplementary Movie 6), suggesting that all three T-type Ca^{2+} channels are involved in ENCC CA. IHC for CaV3.1, CaV3.2 and CaV3.3 (Fig. 3d-f) showed that all three channel types were indeed expressed by ENCCs (Sox10⁺ cells), but not by the surrounding mesenchyme. SAK3 also led to a significant CA increase post-EDNRB blockade with BQ788, but CA remained well below physiological levels, even after 1 day culture (Fig. S14).

We next targeted Cl channels by applying three different classes of inhibitors: 5-Nitro-2-(3-phenylpropylamino)benzoic acid (NPPB), niflumic acid (NFA) and 4,4'-Diisothiocyanato-2,2'-stilbenedisulfonic acid (DIDS). These compounds led to a drastic CA decrease (Figs. 3c and S11, and Supplementary Movie 7) and a retraction of cell processes (Supplementary Movie 7). Transient CA could also be elicited by EDN3 10 μM after 15 min incubation in 100 μM NPPB, but the transients had low amplitude (Fig. S9). NPPB and DIDS systematically induced ENCC death after 24 h (Fig. S15). NFA 50 μM inhibition kinetics were similar to Z944 50 μM (Fig. S12): CA had recovered after 24 h, ENS morphology was normal, and the fraction of dead ENCCs similar to control samples (Fig. S16). Cl channels likely contribute to Ca^{2+} transients by depolarizing the cell membrane through Cl efflux, thereby opening VGCCs^{31,32}. This idea is in line with the fact that the membrane depolarizer 4-AP markedly increased CA (Fig. S13). 4-AP could not however re-stimulate CA post-EDNRB block (Fig. S14c), and also induced cell death after 24 h (Fig. S15).

The purinergic pathway is an important actor of ENCC multicellular Ca^{2+} waves²³. We found that the ATP_e enzymatic degradation inhibitor ARL 67156 and exogenous ATP_e could transiently increase wave activity after EDNRB blockade (Fig. S14d,e). Higher ATP_e concentrations could even result in a network-spanning intracellular Ca^{2+} rise (Fig. S14d and Supplementary Movie 8). These effects were however not sustained in time (Fig. S14e), indicating that the purinergic pathway could not bypass the main regulator EDN3/EDNRB.

Ca^{2+} activity correlates with ENCC migration speed

We next investigated how pharmacological upregulation of CA by EDN3 or SAK3 affected ENCC migration from E11.5 midgut explants embedded in a 3D collagen gel. We found that both EDN3 1 nM and GDNF 10 ng/mL increased migration distances from the explant compared to control conditions, and that they acted synergistically when combined (Fig. 4). Strikingly, we found that the CA activator SAK3 was able to mimic the effect of EDN3, i.e. migration distances were similarly high in GDNF + SAK3 10 μM and GDNF + EDN3 1 nM conditions (Fig. 4).

We next assessed the effect of CA inhibitors on ENCC migration in the colon in full E11.5 guts cultured for 1 day in agarose (a gel not permissive to migration). We found that the four conditions that significantly and long-lastingly (Figs. S12 and 2e) lowered CA - Z944 50 μM , NFA 50 μM , AA 1 mM and BQ788 10 μM - all decreased ENCC migration distances in the colon (Fig. 5a,b). These effects could not be attributed to toxicity, as cell death in most ($n = 49/54$) samples was on the same level as control samples (Fig. S16). Addition of SAK3 to BQ788 did not improve ENCC migration down the colon, consistent with the fact that CA was still very low in these conditions (Fig. S14). These results show that, in addition to the well-known inhibitory effect of BQ788 on ENCC migration^{33,34}, Cl channel and T-type VGCC inhibition also result in a migration defect leading to colonic aganglionosis.

Ca^{2+} activity drives cell contractility and traction force to the extracellular matrix

ENCCs exert a traction force on the tissue as they migrate²⁴, visible in situ as a backflow of mesenchyme (Supplementary Movie 9). Several observations indicated that Ca^{2+} oscillations could modulate this traction force by influencing cell contractility, as in smooth muscle: 1^o) CA blockers led to process retraction and rounding (Fig. 2f,

Supplementary Movie 4,7), indicating a loss of ENCC-extracellular matrix (ECM) traction; 2^o) In a 2D migration assay at x60 magnification, we noticed that Ca^{2+} transient could induce abrupt lamellipodium detachment from the substrate ($n = 4$ such events observed, Fig. S17a, Supplementary Movie 10). This could be driven by actomyosin or by calpain activity³⁵; 3^o) Most Ca^{2+} transients (79/102) in this assay were correlated with an abrupt change of nucleus speed, as measured by deep-learning assisted tracking and by kymographs (Fig. S17b-c, Supplementary Movie 11).

To quantify the force exerted by ENCCs on the ECM, we let ENCCs migrate from E11.5 midgut explants in a collagen gel seeded with fluorescent beads that served as fiducial markers of gel deformation (Fig. 6a inset). The traction force on the collagen scaffold induced bead displacements towards the migration front (Fig. 6, Supplementary Movie 12). Immediately after induction of CA by addition of EDN3 1 nM, the bead speed abruptly increased (Fig. 6, Supplementary Movie 12), and the tip of the migration “fingers” accelerated (Supplementary Movie 12). When EDNRB was blocked by BQ788, the beads suddenly relaxed, indicating a sudden loss of ENCC-ECM traction force (Fig. 6a,b,d, Supplementary Movie 12), and the migration fingers retracted (Supplementary Movie 12). The effect of the T-type Ca^{2+} channel blocker Z944 was similar to that of BQ788, although the decrease in traction force was less pronounced (Fig. 6c,e). This experiment shows that, similarly to endothelin-induced smooth muscle contraction, EDN3 could stimulate Ca^{2+} -dependent actomyosin, increasing the ENCC-ECM traction force necessary for migration, whereas blocking EDNRB or T-type Ca^{2+} channels relaxed it.

Discussion

Endothelins were identified in 1987 as potent modulators of vascular smooth muscle (vSMC) contractility³⁶. When binding to EDNRs on vSMCs, endothelins drive an increase in cytosolic Ca^{2+} mediated both by the release of Ca^{2+} from intracellular stores and by the entry of extracellular Ca^{2+} via CaV1.2 VGCCs^{32,37,38}. The opening of CaV1.2 is favored by the efflux of Cl from the cytosol to the extracellular medium, resulting in membrane depolarization^{31,32}. Increased cytosolic Ca^{2+} leads to calmodulin activation and acto-myosin cross-bridges responsible for vSMC contraction. As the roles of endothelins in blood pressure regulation became more prominent, mutant mice for EDN3^{39,40} and EDNRB⁴¹ mouse were re-examined. The phenotype of these mice came as a surprise: they presented with colonic aganglionosis at birth, a phenotype known as Hirschsprung disease (HD). EDN3/EDNRB has later been identified as a key pathway promoting ENCC proliferation and delaying their differentiation to enteric neurons and glia^{10,42,43}. The EDN3/EDNRB pathway has since then been attributed a dual, “moonlighting” role^{14,44}: regulator of vSMC tone and blood pressure in adult physiology, driver of ENCC proliferation in the embryo. We reveal here that the immediate action of EDN3 on ENCCs is in fact nearly identical to its effect on smooth muscle tone: it triggers Ca^{2+} activity (Figs. 1 and 2), via a very similar molecular route (Figs. 3 and 7) to vSMC, and the increased cytosolic Ca^{2+} oscillations enhance migration (Figs. 4 and 5) by inducing cell contractility (Fig. 6). vSMC contraction leads to vessel constriction; ENCC contraction leads to an increased traction force to the extracellular-matrix, that is necessary for their migration inside the gut mesenchyme. This force is the reason why investigators have found it indispensable to pin⁴⁵ or embed the gut tract during ex-vivo migration assays⁴⁶, as it otherwise leads to tissue shrinkage and improper migration. The traction force is transmitted via $\beta 1$ -integrins (Fig. 7), and ENCC-specific $\beta 1$ -integrin mutants have been shown to present with a HD phenotype⁴⁷⁻⁴⁹. Ca^{2+} signaling defects reduce the traction force of the ENCCs to the extracellular matrix, lowering their migration speed and thus resulting in colonic aganglionosis. Our investigation shows that ENCCs are akin to miniature muscles that contract and crawl in response to a constrictor peptide, endothelin 3.

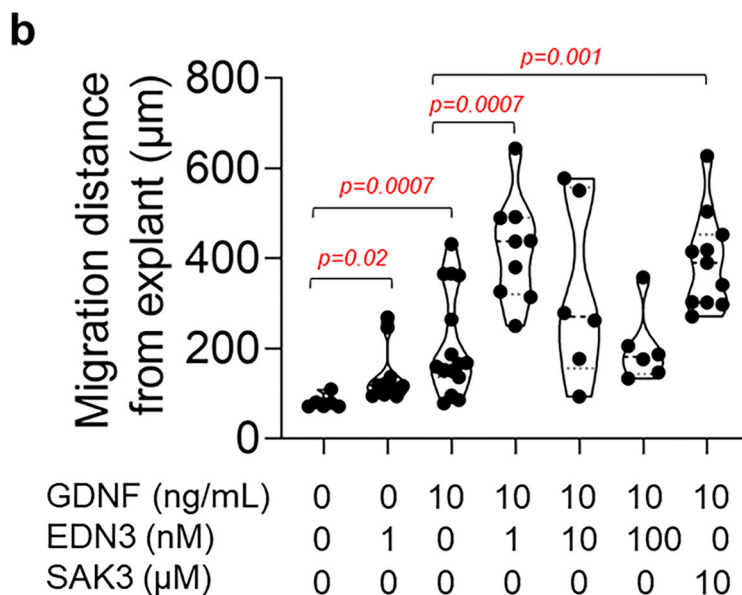
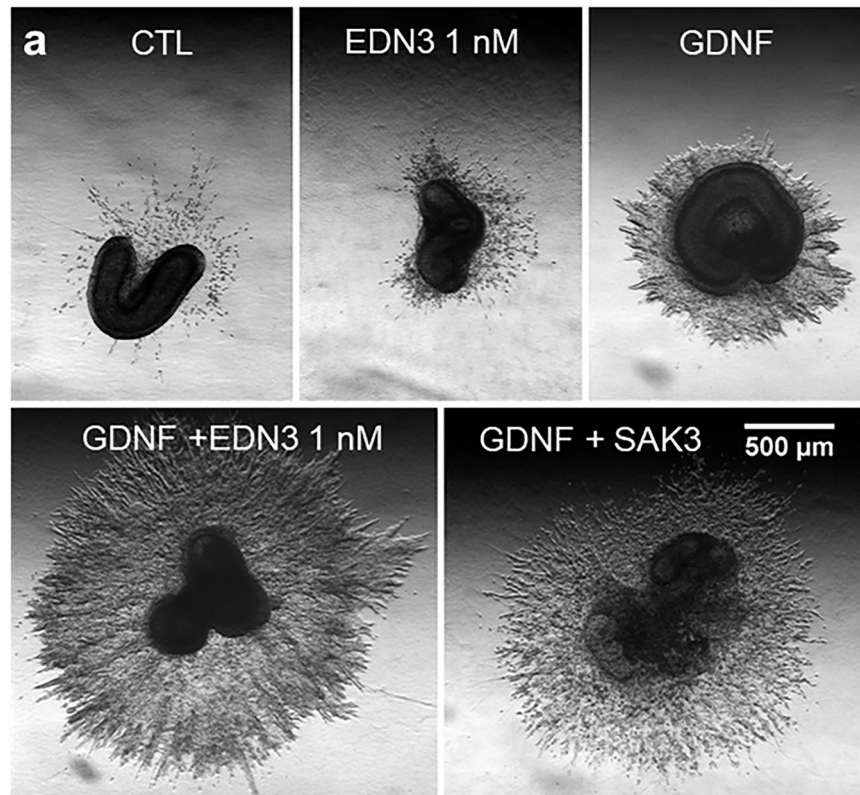


Fig. 4 | Ca^{2+} activity enhances EDN3 and SAK3 promote migration in a collagen gel migration assay. **a** E11.5 midgut explants embedded in a collagen matrix and cultured for 3 days in control, EDN3 1 nM, GDNF 10 ng/mL, GDNF + EDN3 1 nM and GDNF + SAK3 10 μM conditions. ENCC migration in the collagen is visible in brightfield Schlieren-type lighting as a halo of radially oriented cells surrounding

the darker explant. **b** Average migration distance from the explant after 3 days in the different drug conditions, two-tailed Mann-Whitney test. Samples numbers in each group, from left to right, are $n = 6, 10, 15, 9, 6, 6, 11$. Violin plots present the median, upper and lower interquartile range.

It is likely that cytosolic Ca^{2+} oscillations are also involved in the long-term effects of EDN3/EDNRB on ENCC proliferation. ENCC proliferation and migration are inexorably linked – ENCC cannot invade the colon or a collagen gel if they do not also proliferate⁵⁰. Here, we reported macroscopic migration distances (linear in the colon, spherical in the gel) rather than local proliferation rates. EDN3/EDNRB also delays ENCC differentiation^{10,42,43}. Higher CA is generally associated with an undifferentiated state in stem cell cultures^{16,17}. The mitogen

activated protein kinase (MAPK) and the phosphoinositide 3-kinase (PI3K) pathways can both be induced downstream of EDNRB⁵¹, and are dependent on Ca^{2+} activity^{52,53} (Fig. 7). MAPK family members extracellular signal-regulated kinase (ERK) and c-Jun N-terminal kinase (JNK) both promote ENCC migration⁵⁴, and likely also regulate ENCC proliferation and differentiation.

T-type receptor blockade by mibefradil 1 μM was previously reported not to affect ENCC migration²⁸. It is probable that this

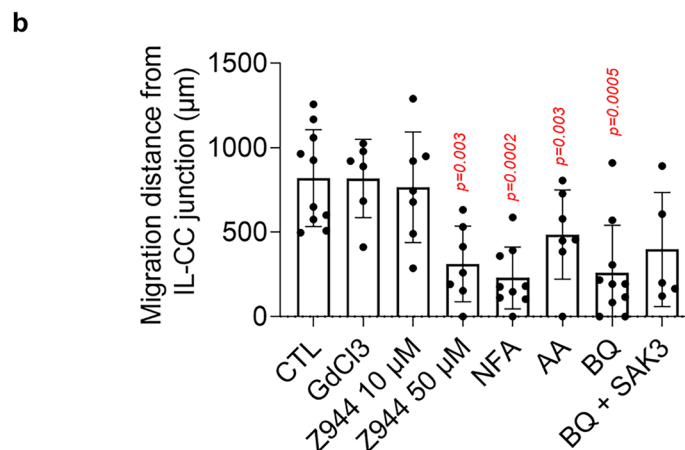
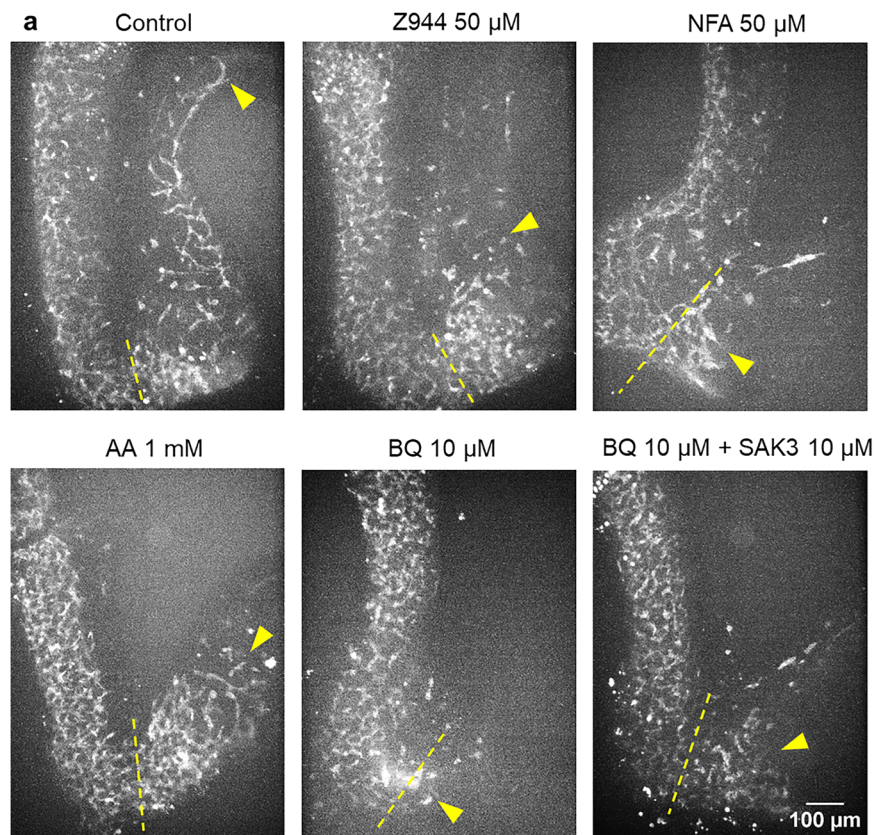


Fig. 5 | Inhibition of Ca^{2+} activity slows down ENCC migration in the cecum and colon. a Maximum projection of GCaMP z-stacks of E11.5 guts cultured for 1 day in control conditions (with DMSO vehicle alone) and in various chemical conditions that alter CA. The dashed yellow line marks the position of the ileocolic junction, and the yellow arrowhead the position of the migration front after 1 day culture. AA= ascorbic acid. **b** Migration distance in the colon from the ileocolic junction

for control ($n=10$), GdCl3 100 μM ($n=6$), Z944 10 μM ($n=7$), Z944 50 μM ($n=7$), NFA 50 μM ($n=9$), AA 1 mM ($n=7$), BQ788 10 μM ($n=10$), BQ788 10 μM + SAK3 10 μM ($n=5$). Two-tailed p -values are shown for the Mann-Whitney test compared to the control group. Z944 50 μM , NFA 50 μM , AA 1 mM and BQ788 10 μM significantly slowed down migration. BQ + SAK3 did not improve migration compared to BQ alone. Error bars are $\pm\text{SD}$.

concentration was insufficient to cause aganglionosis, because the IC₅₀ of mibefradil on isolated cells is 3 μM ⁵⁵; in our experience, effective, sustained blocking of channel activity in whole-gut cultures requires concentrations far above drug IC₅₀ to yield a migration phenotype. Hirst et al.²⁸ also blocked Cl⁻ channels with NPPB 100 μM from an only 100-fold stock solution in a non-specified solvent, and found no effect on migration or on ENCC survival. In our experiments, NPPB 100 μM disrupted CA and migration by systematically inducing ENCC death ($n=11/11$, Fig. S15). The choice of NPPB solvent or inconsistencies in the actual concentrations applied by Hirst et al. may explain the discrepancy. More generally, we were guided in our

choices of pharmacological compounds and concentrations by the Ca^{2+} response, whereas Hirst et al. applied these compounds “blindly” to wildtype guts. Our study differs methodologically from the pioneering work of Hao et al.²³. These investigators focused on multicellular Ca^{2+} waves, with frequencies of $\sim 10^{-4}$ waves/min/100 μm^2 . This is consistent with the wave activity we measure, but ~ 100 - 1000 time more frequent events occur as single-cell transients and are the main form of ENCC CA. We found that, although ATP_e and ARL 67156 can indeed promote multicellular waves²³, they only play a modulatory role in a mechanism that is dominated by EDNRB, Cl⁻ and Ca_v3 channels.

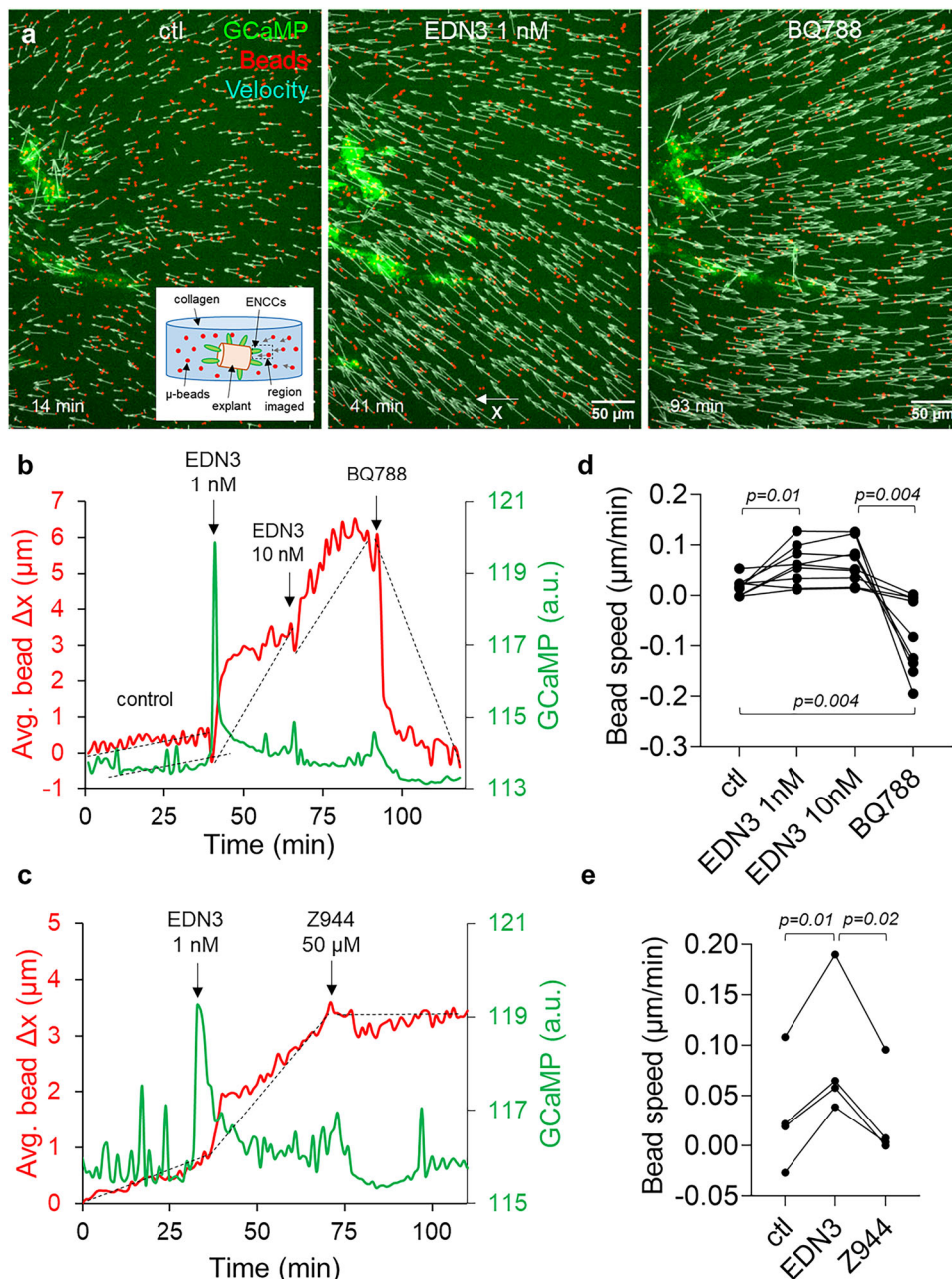


Fig. 6 | Ca^{2+} transients promote migration by increasing ENCC traction force to the extracellular matrix. **a** ENCC 3D migration from an E11.5 midgut explant (to the left, not in the field of view), after 24 h in a collagen matrix with 10 ng/mL GDNF and fiducial marker beads. Maximum projections of z-stacks shows ENCCs to the left (green, GCaMP signal), and AF647 beads (red) inserted in the collagen matrix. The velocity vectors (cyan) are deduced from bead tracking in 1 stack-per-minute videos (Supplementary Movie 12). Left panel: initially, the beads move toward the ENCCs because of the traction force they exert on the collagen gel. The inset shows the experimental setup. Middle panel: the traction force sharply increases when Ca^{2+} rises after EDN3 1 nM administration. Right panel: the traction force inverts (relaxes) after application of BQ788. **b** Average bead x displacement from their

initial x position versus time (red curve), and average GCaMP signal measured in an ROI surrounding the ENCCs (green), in a control, EDN3 1 nM, EDN3 10 nM and BQ788 10 μM sequence and (c) a control, EDN3 1 nM and Z944 50 μM sequence. The average bead displacement was performed over all beads that were not in direct contact with the ENCCs. The average bead speed for each condition is defined as the slope of the dashed lines. Note that the time-resolution of this experiment (1 z-stack per minute) did not allow to resolve in detail the Ca^{2+} transients, but only occasional Ca^{2+} bursts (edn3) or the absence of activity (BQ788, Z944). **d** Average bead speed for $n = 9$ control - EDN3 1 nM - EDN3 10 nM - BQ788 10 μM experiments and (e) $n = 4$ control - EDN3 1 nM - Z944 50 μM experiments, two-tailed paired Student t-test.

CaV3.1 and CaV3.2 expression in E11.5 ENCCs has been previously measured by PCR²⁸; CaV3.2 was found to be ~640 times more expressed than CaV3.1. Our IHC, CA and migration assays indicate that all three CaV3 channel types are present and functional in ENCCs. The CaV3.1 & CaV3.3 agonist SAK3 promoted CA (Fig. 3) and ENCC migration (Fig. 4); the CaV3.2 antagonist ascorbic acid reduced CA (Fig. 3) and ENCC migration (Fig. 5). Very interestingly, a single-

nucleotide polymorphism (SNP) of the *CACNA1H* gene encoding CaV3.2 has been uncovered in a recent HD exome-wide association study¹⁵. Although it is not known whether this point mutation altered CaV3.2 expression or function, our findings suggest it induces HD by altering Ca^{2+} signaling. This motivates further research using dedicated mouse models to better understand the causes of neurocristopathies. We note that the CaV3.2 $^{-/-}$ mouse is viable^{56,57}, although the mutation

induces more pre-natal lethality⁵⁸. It is possible that the surviving CaV3.2 $-/-$ embryos develop compensatory Ca²⁺ influx mechanisms, a common behavior when only one of several protein isoforms is knocked-out⁵⁹.

We found that GDNF and EDN3 (or SAK3) have a synergistic action on ENCC migration from explants (Fig. 3). Our results are in agreement with the findings of Bergeron et al.⁶⁰. We did not observe that EDN3 and GDNF were antagonistic, as has been reported in other studies with mouse²⁵, rat⁶¹ and chicken embryos⁴⁶. These studies were performed respectively at stages E10.5-E11, E13 and E8, at EDN3 concentrations of 100, 20 and 100 nM and after 16 h, 2-3 days and 3 days of migration. It is difficult to fathom the reasons of this discrepancy but we stress that: 1°) migration after 16h²⁵ is too scarce to be precisely quantified, 2°) the EDN3 concentrations applied by other investigators are 1-2 orders of magnitude higher than the maximum pro-CA and pro-migratory effect we report at 1 nM. 1 nM likely reflects the concentration encountered physiologically by ENCCs as they migrate down the gut mesenchyme. We found that CA was not significantly increased at 10 nM EDN3 compared to 1 nM (Figs. 2a and S5c), indicating a saturation effect. Administration of EDN3 10 nM at E12.5 gave rise to a single pan-ENCC transient, which, although impressive, most likely never occurs physiologically. The pan-ENCC Ca²⁺ surge induced by exogenous EDN3 may occur only at E12.5 (and not at E11.5) because of a reduced saturation of EDNRB receptors by endogenous EDN3 at this stage, making it more sensitive to exogenous application.

Edn3 expression is highest in the cecum, with little expression in the hindgut at E12²⁶, which correlates with reduced CA at the ENCC wavefront at E12.5 (Fig. 1). These observations suggest that EDN3 may be most necessary up until the cecum is traversed; slowing down of ENCCs by CA activity inhibitors in our ex-vivo assay (Fig. 5) may have primarily affected migration through the cecum, resulting in a paucity of ENCCs in the colon. Colonic aganglionosis can result from slowed-down ENCC migration at any point of their journey down the gut, not necessarily from slower migration in the colon.

We found that *Is/Is* ENCCs only displayed a ~25% reduction in CA compared to controls. This experiment was performed in the presence of GDNF, serum, and after 1 day culture, all of which can artificially hike CA (Fig. 2e) compared to its in-vivo state. A more refined approach based on GCaMP expressing *Is/Is* mutants would, given our results on the effect of EDNRB blockade, likely reveal a much more drastic CA deficit. Testing the hypothesis that Cl⁻ channels drive an efflux of Cl⁻ ions and a concomitant depolarization (Fig. 5) as in smooth muscle^{31,32} will require electrophysiological measurements. The identification of the Cl⁻ channels involved hinges on the future development of more specific antagonists and agonists: ENCCs express many different Cl⁻ channels²⁸ and several types may be involved. We have not found a correlation between mutations affecting Cl⁻ channels and HD pathogenesis in the literature. This of course does not preempt the fact that they are important for ENCC migration, as such mutations may plainly be lethal. Although our pharmacological approach allowed us to specify CaV3 channels as an important gateway of extracellular Ca²⁺, we cannot at this stage exclude other non-VGCC entry mechanisms, like TRPC⁶².

We deciphered an important mechanism by which endothelin 3 triggers Ca²⁺ activity and contractility

necessary for the migration of enteric neural crest cells. This mechanism is likely to play a more general role in NCC derived melanocytes or Schwann cells and EDNRB-expressing cranial NCCs¹⁴, potentially linking Ca²⁺ activity to other neurocristopathy syndromes³. Melanoma⁷ and neuroblastoma⁶³ are known to recapitulate many NCC traits. T-type Ca²⁺ channel upregulation is associated with melanoma aggressiveness⁶⁴ while Ca²⁺ signaling is altered in neuroblastoma⁶⁵. The endothelin axis is more generally aberrantly expressed in tumors⁶⁶,

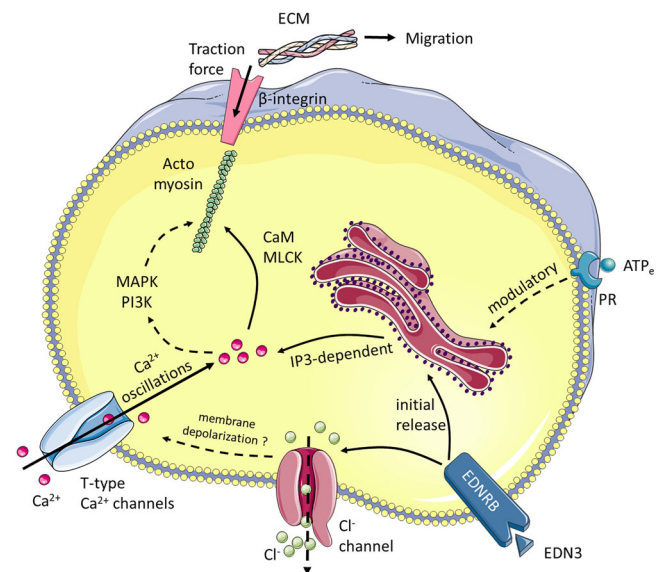


Fig. 7 | Synthetic scheme of the pathways leading to Ca²⁺ transient generation and ENCC migration. PR: purinergic receptor, IP3: inositol trisphosphate, CaM: calmodulin, MLCK: myosin light chain kinase, MAPK: mitogen activated protein kinase, PI3K: phosphoinositide 3-kinase. Dashed arrows indicate mechanistic links for which there is evidence from the literature in related systems. EDNRB activation can trigger a direct release of Ca²⁺ from intercellular stores, but Cl⁻ channels, T-type Ca²⁺ channels and extracellular Ca²⁺ are necessary for sustained Ca²⁺ oscillations. Image elements provided by Servier Medical Art (<https://smart.servier.com>), licensed under CC BY 4.0 (<https://creativecommons.org/licenses/by/4.0/>).

promoting invasion and metastasis: the mechanism we describe here for neural crest cells may also be at play in cancer cell migration.

Methods

Ethics

Mice were hosted at the Institut Jacques Monod (GCaMP) and at the Institut Imagine LEAT (*Is/+* heterozygotes) animal husbandries. They had access to housing, food and water ad-libitum. Temperature in the husbandry was 20–24 °C and humidity in the range 45–55%. The mice were exposed to light from 7 am to 7 pm. Females were kept in common cages with a maximum of 5 females per cage. For mating, the male is introduced in the evening and removed in the morning after detection of plugs in the morning. Pregnant mice were killed by cervical dislocation to retrieve embryos age E10.5 to E12.5. The embryos were separated and immediately beheaded with surgical scissors. The methods used to kill the mice conform to the guidelines of CNRS and INSERM animal welfare committees. Killing of mice for retrieval of embryos is a terminal procedure for which neither CNRS or INSERM assign ethics approval codes hence none are given here.

Mouse gut samples

The Cre reporter mice C57BL/6N-Gt(ROSA)26Sor^{tm1}(CAG-GCaMP6f) Khakh/ mice is referred to as Gcamp6f/fl. A transgenic mouse line in which the transgene is under the control of the 3-kb fragment of the human tissue plasminogen activator (Ht-PA) promoter Tg(PLATcre) 116Sdu16 is referred to as Ht-PA::Cre. Gcamp6f/fl males were crossed with Ht-PA::Cre females to generate embryos carrying the calcium fluorescent reporter in neural crest cells and their derivatives²⁷. The gut of each embryo was dissected in PBS with 1 mM Ca²⁺, 0.5 mM Mg²⁺ and 1% penicillin-streptomycin, from stomach (cut at the oesophagus-stomach junction) to colon (cut at the colon-anus junction). The mesentery of E11.5 guts was kept intact. 57% (118/207 for which the full count was performed) of the embryos expressed GCaMP specifically in

NCCs, while 43 % expressed GCaMP in all cells, with the mesenchymal signal being dominant⁶⁷; these phenotypes could be easily recognized during confocal imaging. We do not know the reason of this partial specificity of GCaMP. Only embryos expressing GCaMP in NCCs were used for Ca²⁺ imaging. Ubiquitously GCaMP expressing embryos, which were otherwise morphologically normal, were used for experiments where Ca²⁺ imaging was not required.

Heterozygous *Is/+* animals were crossed and embryos retrieved at E11.5. DNA extraction and subsequent genotyping were performed from head biopsies of each embryo, using the direct PCR lysis reagent (Viagen). Genotyping was performed using primers (Eurogentec, Belgium) m-Edn3 *Is* F GAC TGT GCC CTA TGG ACT GT and m-Edn3 *Is* R GGT GAC ATC TCT GGT GCG TG^{68,69}.

Organ culture and Ca²⁺ imaging

After dissection, each gut was placed on a pre-solidified 0.5 mL layer of 1% low-melting point agarose (Conalab 8050.11, dissolved in PBS with Ca²⁺ 1 mM and Mg²⁺ 0.5 mM), in a 35 mm diameter Petri dish (Greiner). This gel layer prevents adhesion of the gut and subsequent ENCC migration on the dish bottom, confining it to the organ. The gut was then immobilized by pouring additional 0.5 mL of liquid agarose on top and letting it gel at 4 °C for 10 minutes. Capillary forces of the shallow liquid agarose layer gently press down the gut, most of the time positioning the stomach, midgut and colon in a horizontal plane that was optimal for microscopy. Immobilization is crucial both for Ca²⁺ imaging and to prevent shrinking / retraction of the sample during culture. The 1 mL gut & gel were covered by 2 mL of complemented DMEM:F12 Glutamax (Gibco 31331-028). Final concentrations after diffusion and dilution of the medium in the PBS-based agarose were Ca²⁺ 1 mM, Mg²⁺ 0.5 mM, penicillin-streptomycin 1%, Fetal Veal Serum 6.6 %, while all other molecules that are present in DMEM:F12 but not in PBS (e.g. glucose, amino acids etc.) had their concentration divided by a factor 2/3 compared to DMEM:F12 alone. Samples were incubated at 37 °C in a 5% CO₂ 95% air atmosphere for at least 45 min before imaging.

Calcium imaging was performed on an inverted spinning-disk microscope (Olympus IX-81, Yokogawa CSU-X1) equipped with an ILE laser-base (Andor) and a Zyla camera (Andor, resolution 1392×1040 pixel). The GCaMP signal was excited at 488 nm and the emission filtered at 497-527 nm. Time-lapse videos were recorded at x10 magnification, 400 ms exposure time, 1 Hz acquisition rate, for at least 3 min, and often longer depending on the type of experiment. We did not observe any illumination-induced bleaching or alteration of the sample. Sample basal (endogenous) Ca²⁺ activity was first recorded, and the position of the ENCC wavefront determined by a z-stack at the level of the ileo-caecal junction (E11.5). Drugs were then added from stock solutions directly in the Petri dish, far from the sample, without displacing it, and homogenized by up & down movements with a 1 mL pipette. Products used in this report as well as solvent and stock concentration are listed in Fig. S18. In preliminary experiments, addition of the drug was performed during the time-lapse to capture potential immediate effects. For most drugs, CA was then recorded 10-15 min post-administration. After imaging, samples were placed back in the incubator for further culture. Time-lapse and z-stack imaging was performed after 24 h to assess ENCC wavefront position and CA. Some samples were imaged multiple times during the culture period to assess drug kinetics (Fig. S12). Some samples were fixed and processed for IHC as described below.

The experiment with *Is/Is* embryos required that the ENCCs migrate out of the intestine because Fluo4AM does not penetrate inside the tissue. We achieved this by placing E11.5 explants on 35 mm Greiner Petri dishes and covering them with a thin meniscus of collagen gel (0.5 mL, 1 mg/mL, as described below) to hold them down against the Petri surface. After gelling, the preparation was topped with 2 mL complemented medium with GDNF 10 ng/mL, cultured for

1 day, loaded with 1.8 μM Fluo4-AM for 5 min, and 3 min timelapse movies were recorded in 3 different locations per sample. The samples were immediately fixed after calcium imaging for IHC.

Ca²⁺ activity analysis

Analysis of CA was performed using custom-written ImageJ 1.54r macro and Matlab R2018a scripts, and is synthesized in Fig. S1. Briefly, a fixed mesh comprised of 2745 square regions-of-interest (ROIs), each 250 μm², was overlaid on the 8-bit video. A matrix of the average pixel intensity over time in each square was retrieved and input into Matlab for peak detection. The “findpeaks” function was applied, specifying, to filter out noise, a minimum peak prominence of 2 (8-bit pixel intensity unit), a minimum peak width of 3 sec, a minimum inter-peak time of 3 sec. Illumination and peak filtering settings were identical for all videos acquired, allowing quantitative comparison of GCaMP signal intensity across samples. We measured in each ROI the number of peaks, and, for ROIs in which there was at least one peak, the frequency (number/acquisition time), average duration (width at half-maxima) and average intensity ratio I/I_0 ; the data of all ROIs was collected to generate heatmaps of these variables, assess their spatial distribution, and compute their spatial average. To reflect the general activity of the region imaged, we defined the Ca²⁺ activity $CA = N_{peaks} / (A_{cells} T)$, where N_{peaks} is the total number of transients in a given video, A_{cells} the total area of the GCaMP positive cells within the field of view and T the duration of the acquisition. A_{cells} was determined by first time-projecting the average intensity to obtain a crisp image of the ENCC network, and by then applying iteratively stricter Bernsen local thresholds under ImageJ, stopping just before it diverged (Fig. S1e). A_{cells} should remain constant for an experiment with a fixed z and field of view. Because our procedure yielded some variability depending on Ca²⁺ basal level and activity, we selected for a given experiment the biggest A_{cells} and applied it to all other conditions of this experiment (e.g. before/after drug). CA was expressed in units of events/100 μm²/min; because a cell has typically an area of 100 μm², CA has values lying in the same range as frequencies expressed in cycles-per-minute (cpm).

For *Is/Is* samples, we followed the same procedure but used a finer mesh of 86 μm² (9890 ROIs in total) to gain resolution to differentiate ENCC from mesenchymal CA. After registration of Sox10 & α-SMA IHCs with frequency heatmaps, we drew ROIs around Sox10 positive aggregates using the ImageJ ROI manager, and then measured the average pixel intensity of these ROIs on the greyscale frequency heatmap. The average frequency was obtained by weighing the measured frequency of each aggregate by its area (i.e. bigger aggregates contributed more to the average). Area-weighted frequency and CA are proportional; we present the former in Fig. 2i because the finer mesh size used results in a higher event count compared to the standard mesh used in the remainder of the study.

Collagen gel organ culture

Collagen gels (Figs. 4 and 6) were prepared from Cultrex Rat Collagen I (Bio-Techne) at 1 mg/mL on ice, following the manufacturer's guidelines. For 3D contractility experiments (Fig. 6), fluorescent deep-red 0.2 μm diameter spheres (ThermoFisher, F8807) were added to the mixture at 1:100000 dilution to serve as fiducial tracers. Midgut segments from E11.5 embryos were cut in 2-3 pieces with micro-scissors and each segment was embedded in 1 mL of liquid collagen, that gelled after incubating at 37 °C for 45 min. 2 mL of complemented medium with 10 ng/mL GDNF were then added. Collagen gel migration was assessed after culture for 3 days at 37 °C, in a 5% CO₂ - 95% air humidified atmosphere. We measured the area S_1 occupied by the gut explant and the ENCC halo, the area S_2 occupied by the gut explant alone, and computed the average migration distance from the explant as $\sqrt{S_1/\pi} - \sqrt{S_2/\pi}$. This approach yielded an average radius which took into account halo asymmetries.

Immunohistochemistry

For registration of CA with IHC (Supplementary Movie 2, Fig. 2g,h), guts were fixed in 4% PFA in PBS for 20 min, washed 3 times, then blocked and permeated in 1% BSA and 0.1% triton in PBS for 1 h, immersed in 1:200 mouse monoclonal Anti-SOX10 (Sigma, AMAB91297) for 24 h, washed 3 times, immersed in 1:500 anti-mouse AF647 secondary antibody with 1:500 β III-tubulin FITC conjugated antibody (Abcam 224978) or 1:500 α -SMA Cy3 conjugated antibody (Sigma C6198) for 24 h, washed 3 times in PBS, and imaged in the same location as during calcium imaging. Slight translation and rotation registration corrections between the CA time lapse movie and the IHC were performed manually using the GIMP software.

For IHC of T-type Ca^{2+} channels (Fig. 3d-f), we used explants from the 3D contractility assay (see below). Some of these explants touched the bottom of the Petri-dish and ENCCs can, in addition to the 3D halo, also migrate on the dish surface, as a 2D sheet, which facilitated imaging. After fixation, blocking and permeation, samples were incubated for 1 day in 1:200 mouse Anti-SOX10 and 1:100 rabbit anti CaV3.1 (Alomone Labs #ACC-021) or 1:100 rabbit anti CaV3.2 (Alomone Labs #ACC-025) or 1:100 rabbit anti CaV3.3 (Alomone Labs #ACC-009) for 24 h, washed 3 times, incubated in secondary 1:500 anti-mouse Cy3 and 1:500 anti-rabbit AF647 antibody for another day, washed and imaged. T-type Ca^{2+} channel IHC was only successful when performed on fixed cells that had been induced to emigrate from an explant, without embedding or cutting; we did not observe any specific signal when native E11.5 guts were fixed, cryo-sectioned and labeled, most probably owing to degradation of the proteins when performing these steps.

2D migration assay

For the x60 experiments (Fig. S17), a E11.5 GCaMP midgut explant was cultured on a Petri dish with a culture surface-treated polymer coverslip bottom (Ibidi 81156), immobilized with a 500 μL meniscus of 1% low-melting point agarose gel, and cultured one day in complemented medium with 10 ng/mL GDNF. Numerous ENCCs migrated out on the coverslip and were imaged at x60 magnification at 1 Hz, for 10 to 30 min. Cell nuclei appeared as dark spots surrounded by brighter cytoplasm. They were tracked using the deep-learning Segment Anything Model 2 (SAM2) developed by Meta and implemented under QuPath⁷⁰. Nucleus boundary and centroid tracking were very precise (Supplementary Movie 11). Nucleus centroid position was plotted together with the GCaMP signal obtained from ROI intensity measurements of the cytoplasm of the tracked cell. Kymographs were obtained with the ImageJ Reslice function performed along a rectangle encompassing the cell trajectory.

3D contractility assay

3D contractility experiments were performed after 1-2 day of culture in collagen gel seeded with beads (see above), at x20 magnification, acquiring z-stacks in the bulk of the gel in GFP (cells) and AF647 (beads) with a step of 2 μm over a thickness of 30-50 μm every minute for up to 120 min. Drugs were added during the time-lapse and mixed very carefully to not perturb bead positions. The z&t stacks of the cells (GFP) and beads (AF647) were first z max-projected to yield t-stacks (time-lapse). The bead t-stack was flat-field corrected (Biovoxxel toolbox under Fiji), smoothed (Gaussian blur radius 2), thresholded (Li Auto Threshold) and the initial bead positions were measured using the ImageJ Analyze Particles tool. These initial coordinates were fed into the Tracker plugin (developed by our colleague O. Cardoso) to yield the coordinates of each bead at each time point. Inconsistent tracking was filtered out by applying conditions on the maximum rate of displacement. The average displacement of beads from their initial position towards the ENCC migration front was computed.

Statistics and Reproducibility

All sample numbers indicated in this report correspond to different embryos (guts, biological replicates). Except for Is/Is experiments which were performed on 2 litters, data for all other experiments was collected from at least 3 different litters and technically replicated at least 3 times, i.e. they were performed on 3 different days with fresh samples following the same procedure each time. Experiments on Is/Is were performed blindly, i.e., the genotype was known after data collection and analysis. In all other experiments, blinding was not possible and not relevant to this study. The sample size range is $n = 5-23$ and was determined according to the type and variability of experiment results. p -values reported correspond to statistical tests mentioned in the figure legends. All instances of the WMP test are two-tailed.

Reporting summary

Further information on research design is available in the Nature Portfolio Reporting Summary linked to this article.

Data availability

Essential data generated or analyzed during this study are included in the manuscript and supporting files. Source data are provided with this paper. Other non-essential data are available from the corresponding author upon request. Source data are provided with this paper.

Code availability

Essential codes for calcium imaging analysis are provided as supporting files.

References

1. Le Douarin, N. M. & Dupin, E. The Neural Crest, a Fourth Germ Layer of the Vertebrate Embryo: Significance in Chordate Evolution. *Neural Crest Cells Evol. Dev. Dis.* 3–26 (2014). <https://doi.org/10.1016/B978-0-12-401730-6.00001-6> (2014).
2. Bolande, R. The neurocristopathies: unifying concept of disease arising in neural crest maldevelopment. *Hum. Pathol.* **5**, 409–429 (1974).
3. Vega-Lopez, G. A., Cerrizuela, S., Tribulo, C. & Aybar, M. J. Neurocristopathies: New insights 150 years after the neural crest discovery. *Dev. Biol.* **444**, S110–S143 (2018).
4. Wilkins, A. S., Wrangham, R. W. & Tecumseh Fitch, W. The ‘domestication syndrome’ in mammals: A unified explanation based on neural crest cell behavior and genetics. *Genetics* **197**, 795–808 (2014).
5. Librado, P. et al. Ancient genomic changes associated with domestication of the horse. *Sci. (80-)* **356**, 442–445 (2017).
6. Bailey, C. M., Morrison, J. A. & Kulesa, P. M. Melanoma revives an embryonic migration program to promote plasticity and invasion. *Pigment Cell Melanoma Res.* **25**, 573–583 (2012).
7. Diener, J. & Sommer, L. Reemergence of neural crest stem cell-like states in melanoma during disease progression and treatment. *Stem Cells Transl. Med.* **10**, 522–533 (2021).
8. Yu, Q. et al. Sacral neural crest-independent origin of the enteric nervous system in mouse. *Gastroenterology* **166**, 1085–1099 (2024).
9. Lake, J. I. & Heuckeroth, R. O. Enteric nervous system development: Migration, differentiation, and disease. *Am. J. Physiol. - Gastrointest. Liver Physiol.* **305**, 1–24 (2013).
10. Mwizerwa, O. et al. Gdnf is mitogenic, neurotrophic, and chemoattractive to enteric neural crest cells in the embryonic colon. *Dev. Dyn.* **240**, 1402–1411 (2011).
11. Young, H. M. et al. GDNF is a chemoattractant for enteric neural cells. *Dev. Biol.* **229**, 503–516 (2001).
12. Anderson, R. B., Newgreen, D. F. & Young, H. Neural Crest and the Development of the Enteric Nervous System. (2013).

13. Bondurand, N., Dufour, S. & Pingault, V. News from the endothelin-3/EDNRB signaling pathway: Role during enteric nervous system development and involvement in neural crest-associated disorders. *Dev. Biol.* **444**, S156–S169 (2018).
14. Kanai, S. M. & Clouthier, D. E. Endothelin signaling in development. *Dev.* **150**, (2023).
15. Tang, W. et al. Exome-Wide Association Study Identified New Risk Loci for Hirschsprung's Disease. *Mol. Neurobiol.* **54**, 1777–1785 (2017).
16. Sundelacruz, S., Levin, M. & Kaplan, D. L. Role of membrane potential in the regulation of cell proliferation and differentiation. *Stem Cell Rev. Reports.* <https://doi.org/10.1007/s12015-009-9080-2> (2009).
17. Torre, E. C., Bicer, M., Cottrell, G. S., Widera, D. & Tamagnini, F. Time-dependent reduction of calcium oscillations in adipose-derived stem cells differentiating towards adipogenic and osteogenic lineage. *Biomolecules* **11**, 1400 (2021).
18. Yang, M. & Brackenbury, W. J. Membrane potential and cancer progression. *Frontiers in Physiology* <https://doi.org/10.3389/fphys.2013.00185> (2013).
19. Carey, M. B. & Matsumoto, S. G. Spontaneous calcium transients are required for neuronal differentiation of murine neural crest. *Dev. Biol.* **215**, 298–313 (1999).
20. Morokuma, J. et al. Modulation of potassium channel function confers a hyperproliferative invasive phenotype on embryonic stem cells. *Proc. Natl. Acad. Sci. Usa.* **105**, 16608–16613 (2008).
21. Follmer, M. L., Isner, T., Ozekin, Y. H., Levitt, C. & Bates, E. A. Depolarization induces calcium-dependent BMP4 release from mouse embryonic palate mesenchyme. *bioRxiv* 2024.06.11.598333 <https://doi.org/10.1038/s41467-024-53642-2> (2024).
22. Ferreira, F., Moreira, S., Zhao, M. & Barriga, E. H. Stretch-induced endogenous electric fields drive directed collective cell migration in vivo. *Nat. Mater.* 2025 243 **24**, 462–470 (2025).
23. Hao, M. M. et al. Spontaneous calcium waves in the developing enteric nervous system. *Dev. Biol.* **428**, 74–87 (2017).
24. Chevalier, N. R. et al. How tissue mechanical properties affect enteric neural crest cell migration. *Sci. Rep.* **6**, 20927 (2016).
25. Barlow, A., De Graaff, E. & Pachnis, V. Enteric Nervous System Progenitors Are Coordinately Controlled by the G Protein-Coupled Receptor EDNRB and the Receptor Tyrosine Kinase RET. *Neuron* **40**, 905–916 (2003).
26. Leibl, M. A. et al. Expression of endothelin 3 by mesenchymal cells of embryonic mouse caecum. *Gut* **44**, 246–252 (1999).
27. Amedzrovi Agbesi, R. J., El Merhie, A., Spencer, N. J., Hibberd, T. & Chevalier, N. R. Tetrodotoxin-resistant mechanosensitivity and L-type calcium channel-mediated spontaneous calcium activity in enteric neurons. *Exp. Physiol.* **109**, 1545–1556 (2024).
28. Hirst, C. S. et al. Ion channel expression in the developing enteric nervous system. *PLoS One* **10**, (2015).
29. Nelson, M. T. et al. Molecular mechanisms of subtype-specific inhibition of neuronal T-type calcium channels by ascorbate. *J. Neurosci.* **27**, 12577–12583 (2007).
30. Yabuki, Y. et al. Pharmacological properties of SAK3, a novel T-type voltage-gated Ca²⁺ channel enhancer. *Neuropharmacology* **117**, 1–13 (2017).
31. Takenaka, T. et al. Attenuation of endothelin effects by a chloride channel inhibitor, indanyloxyacetic acid. *Am. J. Physiol.* **262**, (1992).
32. Wray, S., Prendergast, C. & Arrowsmith, S. Calcium-activated chloride channels in myometrial and vascular smooth muscle. *Front. Physiol.* **12**, (2021).
33. Young, H. M. et al. Colonizing while migrating: how do individual enteric neural crest cells behave? *BMC Biol.* **12**, 23 (2014).
34. Woodward, M. N., Kenny, S. E., Vaillant, C., Lloyd, D. A. & Edgar, D. H. Time-dependent effects of endothelin-3 on enteric nervous system development in an organ culture model of Hirschsprung's disease. *J. Pediatr. Surg.* **35**, 25–29 (2000).
35. Franco, S. J. et al. Calpain-mediated proteolysis of talin regulates adhesion dynamics. *Nat. Cell Biol.* **6**, 977–983 (2004).
36. Barton, M. & Yanagisawa, M. Endothelin: 30 years from discovery to therapy. *Hypertension* **74**, 1232–1265 (2019).
37. Sudjarwo, S. A., Hori, M. & Karaki, H. Effect of endothelin-3 on cytosolic calcium level in vascular endothelium and on smooth muscle contraction. *Eur. J. Pharmacol.* **229**, 137–142 (1992).
38. Haynes, W. G., Strachan, F. E. & Webb, D. J. Endothelin ETA and ETB receptors cause vasoconstriction of human resistance and capacitance vessels in vivo. *Circulation* **92**, 357–363 (1995).
39. Lane, P. W. Association of megacolon with two recessive spotting genes in the mouse. *J. Hered.* **57**, 29–31 (1966).
40. Baynash, A. G. et al. Interaction of endothelin-3 with endothelin-B receptor is essential for development of epidermal melanocytes and enteric neurons. *Cell* **79**, 1277–1285 (1994).
41. Garipey, C. E., Cass, D. T. & Yanagisawa, M. Null mutation of endothelin receptor type B gene in spotting lethal rats causes aganglionic megacolon and white coat color. *Proc. Natl. Acad. Sci. Usa.* **93**, 867–872 (1996).
42. Lahav, R. et al. Endothelin 3 selectively promotes survival and proliferation of neural crest-derived glial and melanocytic precursors in vitro. *Proc. Natl. Acad. Sci. Usa.* **95**, 14214–14219 (1998).
43. Natarajan, D., Grigoriou, M., Marcos-Gutierrez, C. V., Atkins, C. & Pachnis, V. Multipotential progenitors of the mammalian enteric nervous system capable of colonising aganglionic bowel in organ culture. *Development* **126**, 157–168 (1999).
44. Chevalier, N. Physical organogenesis of the gut. *Development* **149**, dev200765 (2022).
45. Hearn, C. J., Young, H. M., Ciampoli, D., Lomax, A. E. G. & Newgreen, D. Catenary cultures of embryonic gastrointestinal tract support organ morphogenesis, motility, neural crest cell migration, and cell differentiation. *Dev. Dyn.* **214**, 239–247 (1999).
46. Nagy, N. & Goldstein, A. M. Endothelin-3 regulates neural crest cell proliferation and differentiation in the hindgut enteric nervous system. *Dev. Biol.* **293**, 203–217 (2006).
47. Breau, M. et al. Lack of beta1 integrins in enteric neural crest cells leads to a Hirschsprung-like phenotype. *Development* **133**, 1725–1734 (2006).
48. Gazquez, E. et al. Endothelin-3 stimulates cell adhesion and cooperates with β 1-integrins during enteric nervous system ontogenesis. *Sci. Rep.* **6**, 37877 (2016).
49. Chevalier, N. R. et al. A neural crest cell isotropic-to-nematic phase transition in the developing mammalian gut. *Commun. Biol.* **4**, 770 (2021).
50. Simpson, M. J., Zhang, D. C., Mariani, M., Landman, K. A. & Newgreen, D. F. Cell proliferation drives neural crest cell invasion of the intestine. *Dev. Biol.* **302**, 553–568 (2007).
51. Halaka, M. et al. Differences in endothelin B receptor isoforms expression and function in breast cancer cells. *J. Cancer* **11**, 2688 (2020).
52. White, C. D. & Sacks, D. B. Regulation of MAP kinase signaling by calcium. *Methods Mol. Biol.* **661**, 151–165 (2010).
53. Ghigo, A., Laffargue, M., Li, M. & Hirsch, E. PI3K and Calcium Signaling in Cardiovascular Disease. *Circ. Res.* **121**, 282–292 (2017).
54. Goto, A. et al. GDNF and endothelin 3 regulate migration of enteric neural crest-derived cells via protein kinase A and Rac1. *J. Neurosci.* **33**, 4901–4912 (2013).
55. Mehrke, G., Zong, X., Flockerzi, V. & Hofmann, F. The Ca⁺⁺-channel blocker Ro 40-5967 blocks differently T-type and L-type Ca⁺⁺ channels - PubMed. *J. Pharm. Exp. Ther.* **271**, 1483–1488 (1994).
56. Wang, R. & Lewin, G. R. The Cav3.2 T-type calcium channel regulates temporal coding in mouse mechanoreceptors. *J. Physiol.* **589**, 2229–2243 (2011).

57. Chen, C. C. et al. Abnormal coronary function in mice deficient in $\alpha 1H$ T-type Ca^{2+} channels. *Sci. (80-)* **302**, 1416–1418 (2003).
 58. Alpdogan, S., Clemens, R., Hescheler, J., Neumaier, F. & Schneider, T. Non-Mendelian inheritance during inbreeding of Cav3.2 and Cav2.3 deficient mice. *Sci. Rep.* **10**, (2020).
 59. Baghdadi, M. B. et al. PIEZO-dependent mechanosensing is essential for intestinal stem cell fate decision and maintenance. *Science (80-)*. **386**, (2024).
 60. Bergeron, K. F. et al. Male-biased aganglionic megacolon in the TashT mouse line due to perturbation of silencer elements in a large gene desert of chromosome 10. *PLoS Genet.* **11**, (2015).
 61. Kruger, G. M. et al. Temporally distinct requirements for endothelin receptor B in the generation and migration of gut neural crest stem cells. *Neuron* **40**, 917–929 (2003).
 62. Shim, S. et al. Calcium dynamics at the neural cell primary cilium regulate Hedgehog signaling-dependent neurogenesis in the embryonic neural tube. *Proc. Natl. Acad. Sci. USA.* **120**, (2023).
 63. Johnsen, J. I., Dyberg, C. & Wickström, M. Neuroblastoma—a neural crest derived embryonal malignancy. *Front. Mol. Neurosci.* **12**, 9 (2019).
 64. Barceló, C. et al. T-type calcium channels: a potential novel target in melanoma. *Cancers (Basel)* **12**, 391 (2020).
 65. Lange, I., Koster, J. & Koomoa, D. L. T. Calcium signaling regulates fundamental processes involved in Neuroblastoma progression. *Cell Calcium* **82**, (2019).
 66. Rosanò, L., Spinella, F. & Bagnato, A. Endothelin 1 in cancer: Biological implications and therapeutic opportunities. *Nat. Rev. Cancer* **13**, 637–651 (2013).
 67. Chevalier, N. R. et al. Calcium wave dynamics in the embryonic mouse gut mesenchyme: impact on smooth muscle differentiation. *Commun. Biol.* **7**, 1277 (2024).
 68. Stanchina, L. et al. Interactions between Sox10, Edn3 and Ednr β during enteric nervous system and melanocyte development. *Dev. Biol.* **295**, 232–249 (2006).
 69. Rice, J. et al. Transgenic rescue of aganglionosis and piebaldism in lethal spotted mice. *Dev. Dyn.* **217**, 120–132 (2000).
 70. Sugawara, K. Training deep learning models for cell image segmentation with sparse annotations. *bioRxiv* 2023.06.13.544786 <https://doi.org/10.1101/2023.06.13.544786> (2023).
- Model under QuPath, Vincent Fleury, Michael Levin, Alexandre Ayed, Nathalie Rouach, Isabelle Arnoux, Olivier Romito and Master 2 students of the Université Paris Cité Biomedical Engineering 2024-2025 program for thoughtful discussions and/or performing experiments together.

Author contributions

NRC led the project, obtained funding, performed experiments, analyzed data, synthesized data, wrote the draft and revised the paper; TS implemented new analysis methods and analyzed data; ZC performed experiments and analyzed data; NB, FG, MF, AEM, LC, MD, ILP, LZ performed experiments; LZ critically discussed the data; NB revised the draft.

Competing interests

The authors declare no competing interests.

Additional information

Supplementary information The online version contains supplementary material available at <https://doi.org/10.1038/s41467-025-68121-5>.

Correspondence and requests for materials should be addressed to Nicolas R. Chevalier.

Peer review information *Nature Communications* thanks Nandor Nagy and the other anonymous reviewer for their contribution to the peer review of this work. A peer review file is available.

Reprints and permissions information is available at <http://www.nature.com/reprints>

Publisher's note Springer Nature remains neutral with regard to jurisdictional claims in published maps and institutional affiliations.

Open Access This article is licensed under a Creative Commons Attribution 4.0 International License, which permits use, sharing, adaptation, distribution and reproduction in any medium or format, as long as you give appropriate credit to the original author(s) and the source, provide a link to the Creative Commons licence, and indicate if changes were made. The images or other third party material in this article are included in the article's Creative Commons licence, unless indicated otherwise in a credit line to the material. If material is not included in the article's Creative Commons licence and your intended use is not permitted by statutory regulation or exceeds the permitted use, you will need to obtain permission directly from the copyright holder. To view a copy of this licence, visit <http://creativecommons.org/licenses/by/4.0/>.

© The Author(s) 2026

Acknowledgements

This manuscript is dedicated to Jürgen Langenbach, long-time science journalist at Die Presse, and to the memory of Prudence Dulormne. This research was funded by the Agence Nationale de la Recherche ANR GASTROMOVE - ANR-19-CE30-0016-01, by the Université de Paris IDEX Emergence en Recherche CHEVA19RDX-MEUP1, by the CNRS PEPS INSIS "COXHAM" grant, by the Labex "Who AM I?" ANR-11-LABX-0071, and by the Imaging platform BioEmergences-IBiSA, ANR-10-INBS-04 and ANR-11-EQPX-0029. We thank Sylvie Dufour for providing the HtPA::Cre mouse line, Ko Sugarawa for help with the Segment Anything